Acta Pharmaceutica Sinica B 2026;16(3):1733−1746

Chinese Pharmaceutical Association
Institute of Materia Medica, Chinese Academy of Medical Sciences

Acta Pharmaceutica Sinica B

www.elsevier.com/locate/apsb
www.sciencedirect.com

ORIGINAL ARTICLE

Ferroptosis-based nano-assembly enhanced breast cancer therapy by inhibiting intratumor bacteria

Yao Qi[†], Yue Qiu[†], Yuting Zhang, Liang Zhang, Hui Xiong[*], Jing Yao[*]

Department of Pharmaceutics, China Pharmaceutical University, Nanjing 210009, China

Received 19 February 2025; received in revised form 25 June 2025; accepted 26 June 2025

KEY WORDS

Intracellular bacteria;
Breast cancer;
Ferroptosis therapy;
Phototherapy;
Intracellular biological oxidation-reduction cascade reaction;
F-actin;
Pseudopodia;
Inflammatory factors

Abstract Intratumoral bacteria, especially Gram-positive bacteria (G^+), have a unique bacterial niche in breast cancer that promoted tumor progression. However, the effects of G^+ have so far been overlooked, serving an "invisible driver" of breast cancer. Moreover, due to the altered biological structure of G^+ in tumor cells and the penetration barrier of antibiotics, the effect of antibiotic-mediated eradication of G^+ in tumors is limited. Here, to simultaneously inhibit intratumoral G^+ and tumor cells *via* ferroptosis therapy, an amorphous nano-assembly (DFTV) was constructed by assembling doxorubicin (DOX), tannic acid (TA), $FeSO_4$, and vancomycin (Van). DFTV treatment effectively targets intratumoral G^+, thereby inhibiting the growth of the breast tumor and postoperative recurrence by downregulating the expression of inflammatory cytokines, including interleukin-6 (IL-6), interleukin-1β (IL-1β), and tumor necrosis factor-alpha (TNF-α). Moreover, inhibiting intracellular G^+ also restrains the reorganization of F-actin to form pseudopodia, thereby impairing tumor cell motility and blocking metastasis. Collectively, DFTV improves the antitumor efficacy by targeting G^+ in breast tumors, offering novel insights into overcoming the limitations associated with the lack of intratumoral antibacterial therapy in clinical breast cancer treatment protocols.

*Corresponding authors.
E-mail addresses: yaojing@cpu.edu.cn (Jing Yao), 1620174410@cpu.edu.cn (Hui Xiong).
[†]These authors made equal contributions to this work.

Peer review under the responsibility of Chinese Pharmaceutical Association and Institute of Materia Medica, Chinese Academy of Medical Sciences.

https://doi.org/10.1016/j.apsb.2026.01.027

1. Introduction

Abundant commensal Gram-positive bacteria (G^+) are active in breast cancer[1]. Especially, intratumor-resident G^+ are viable and localize within breast cancer cells[2]. These G^+ can activate the Toll-like receptor (TLR2)−NF-κB pathway and stimulate interleukin-6 (IL-6) secretion *via* their characteristic peptidoglycan (PGN) component, finally inducing tumor progression[3,4]. Moreover, bacteria in tumor cells can remodel the cytoskeleton by severing and polymerizing F-actin, thereby facilitating breast cancer cell migration and invasion[5−7]. Thus, to address this vulnerability in breast cancer therapy, tumor-targeted antibacterial therapy for inhibiting intratumoral G^+ is indispensable. However, these intracellular bacteria can establish a unique intracellular niche to evade the immune system and antibiotic therapy by entering host cells[8]. Furthermore, cell wall-deficient bacteria have been observed within the cytoplasm of tumor cells[2]. This compromises the efficacy of even potent G^+ targeting antibiotic vancomycin (Van), since Van's antibacterial effect partly depends on inhibiting bacterial cell wall synthesis[9,10]. In this case, the intratumor-resident G^+ can tolerate systemic administration of multiple-dose Van and may even cause tumor immunosuppression by unexpected destruction of intestinal microbiota homeostasis[11-13].

Attractively, ferroptosis showed the advantages of antibacterial therapy since bacteria typically have low levels of intracellular reducing substances[14,15]. Ferroptosis can utilize iron to generate toxic oxygen intermediates, *e.g.*, hydroxyl radicals (·OH) and hydrogen peroxide (H_2O_2) through the Fenton reaction, finally accelerating unrestrained lipid peroxidation process on the bacterial membrane to eradicate bacteria[16,17]. Notably, even for bacteria that invaded cells, ferroptosis can successfully induce bacterial death[17], thereby helping overcome the above challenges of antibacterial therapy against intratumoral bacteria. Moreover, breast tumor cells are susceptible to ferroptosis therapy due to their iron dependency and the engagement of ferroptosis in the activity of multiple tumor suppressors[18,19]. Accordingly, ferroptosis therapy exerts a dual antitumor effect by simultaneously inhibiting intratumoral G^+ and breast tumor cells.

Herein, to effectively target intratumoral G^+ and thereby overcome tumor recurrence and metastasis driven by tumor-resident bacteria, we designed a self-assembled amorphous nano-assembly (DFTV) by assembling doxorubicin (DOX), tannic acid (TA), $FeSO_4$, and Van (Scheme 1A). In DFTV, DOX, $FeSO_4$, and TA synergistically amplify ferroptosis therapy by triggering intracellular free radical cascade reactions. Benefiting from the unique self-assembly process of DOX, $FeSO_4$, and TA, DFTV could further induce photothermal therapy (PTT) as previously reported[20]. Correspondingly, DFTV strengthened the antibacterial effect of Van against G^+ in breast cancer as well as induced ferroptosis in breast tumor cells (Scheme 1B). DFTV + Laser, which represented DFTV with laser irradiation triggered PTT, mediated strong ferroptosis therapy and displayed an antibacterial efficiency

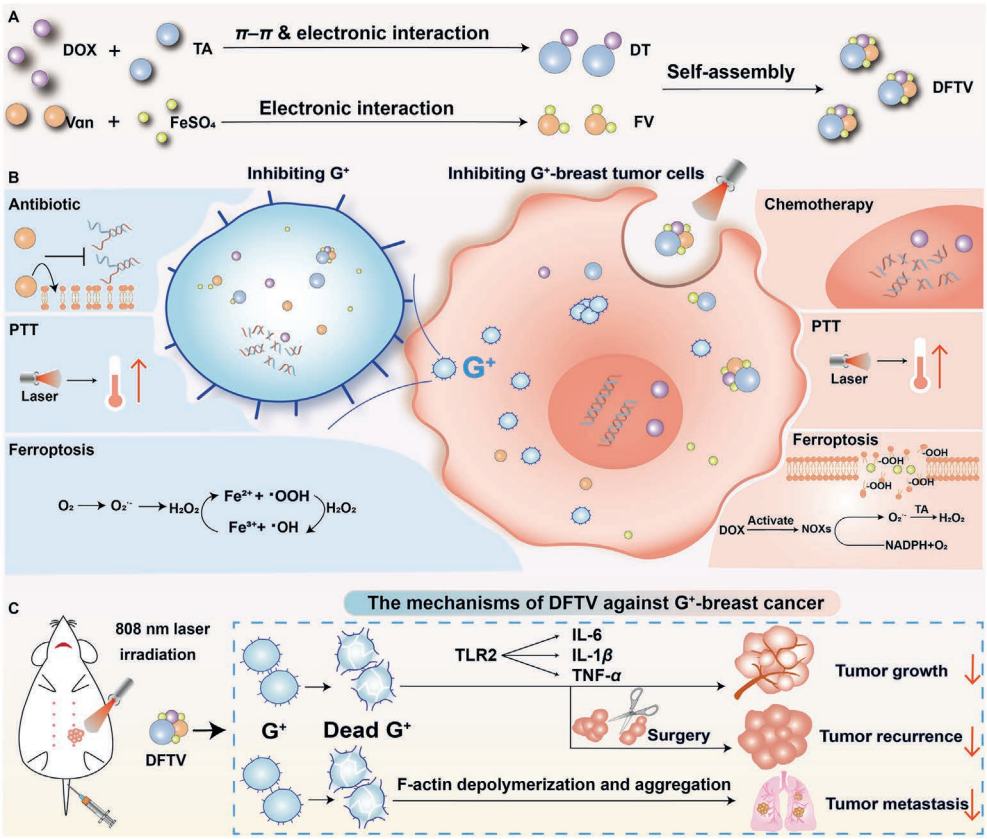

Scheme 1 (A) Schematic illustration of DFTV self-assembly *via* a two-step process. DT denotes self-assembly complex of DOX and TA and FV represents self-assembly complex of Fe^{2+} and Van. (B) Dual-inhibiting therapeutic mechanism of DFTV against intracellular G^+ and breast tumor cells. (C) DFTV inhibits TLR2-IL-6, IL-1β, and TNF-α pathways and remodels tumor cytoskeletal proteins for antitumor growth, recurrence, and metastasis.

of 99.94% and 98.90% against G^+ in primary breast cancer and recurrent breast cancer, respectively. Importantly, the potent antibacterial effect of DFTV against G^+ in breast cancer led to downregulation of pro-tumorigenic and pro-recurrent inflammatory cytokines, including IL-6, IL-1β, and TNF-α. Meanwhile, the cytoskeletal protein F-actin, which would form cellular pseudopods to promote hypermotility of G^+-colonized breast tumor cells, was also inhibited (Scheme 1C). Based on this, breast cancer proliferation and metastasis pathway blocking effects obtained by removing G^+, DFTV + Laser achieved a tumor growth inhibition ratio of 92.99% against G^+-colonized primary breast cancer and demonstrated potent efficacy in inhibiting tumor lung metastasis and postoperative recurrence.

2. Materials and methods

2.1. Materials

Van, ferrous sulfate heptahydrate, TA, deferiprone (DFP), and ferrostatin-1 (Fer-1) were purchased from Aladdin Biochemical Technology Co., Ltd. (Shanghai, China); DOX was purchased from Shengli De Biotechnology Co., Ltd. (Nanjing, China); gentamicin sulfate was purchased from Yuanye Bio-technology Co., Ltd. (Shanghai, China); ELISA kits, Cell Counting Kit-8, DCFH-DA probe, total superoxide dismutase (SOD) assay kits and Liperfluo fluorescent probe were purchased from Beyotime Biotechnology Co., Ltd. (Shanghai, China); anti-F-actin antibody (bs-1571R, Bioss, Woburn, MA, USA); anti-GPX4 antibody bs-3884R, Bioss, Woburn, MA, USA); BALB/c mice were purchased from Cavens Experimental Animal Co., Ltd. (Taizhou, China). All animal experiments were approved by the Institutional Animal Care and Use Committee of China Pharmaceutical University (approval No. 2022-05-059).

2.2. Preparation of DFTV

Firstly, TA solution (1 mL, 4.0 mg/mL) was added to DOX solution (1 mL, 4.0 mg/mL), and $FeSO_4$ solution (1 mL, equivalent to Fe^{2+} 6.0 mg/mL) was added to Van solution (1 mL, 7.0 mg/mL). Then, the above solutions were mixed and stirred to prepare DFTV pre-assembly. DFTV nano-assembly was collected through centrifugation at 10,000 rpm (TDZ5-WS, Centrifuge Xiangyi, Changsha, China) for 10 min, followed by probe sonication at 200 W for 10 min. The particle size of DFTV nano-assembly was analyzed by dynamic light scattering (DLS, Malvern Instruments, Malvern, UK). Transmission electron microscopy (TEM, Hitachi, Tokyo, Japan) was used to characterize the morphology of DFTV. The crystallinity of DFTV was determined using an X-ray diffraction (XRD) instrument (D8 Advance, Bruker AXS GmbH, Karlsruhe, Germany). UV−Vis spectrophotometer (TU-1810PC spectrophotometer, Purkinje General Instrument Co., Ltd., Beijing, China), fluorescence spectrophotometer (Shimadzu RF-5301PC, Kyoto, Japan), and fourier transform infrared spectrometer (FTIR, Bruker, Tensor 27, Billerica, MA, USA) were employed to investigate the assembly mechanism of DFTV. Monolith NT.115 (NanoTemper Technologies, Munich, Germany) was utilized to determine the binding affinity strength of DOX, TA, $FeSO_4$, and Van. Differential scanning calorimetry (DSC, 204 F1 Phoenix®, NETZSCH, Selb, Germany) was employed to characterize the interaction and position relationship of DFTV.

2.3. The method for establishing G^+-colonized 4T1 (G^+-4T1) cells

The G^+ were cultured to the logarithmic growth phase. Then, 4T1 cells were infected with G^+ at a multiplicity of infection (MOI) of 2 for 12 h. The cells were incubated with 200 μg/mL gentamicin sulfate for 2 h to eliminate the extracellular G^+. To count the colonies of G^+, the lysate of G^+-4T1 cells was plated on blood agar plates.

2.4. G^+-4T1 cells viability and migration ability

The viability of 4T1 cells after being infected with G^+ was tested by cell counting kit-8 (CCK-8). G^+-4T1 cells and 4T1 cells were seeded at a density of 10^4 cells/well. To prevent the proliferation of extracellular bacteria, 200 μg/mL gentamicin sulfate was added to the medium. Finally, 10% CCK-8 solution was added and incubated for 2 h. The optical density (OD) at 450 nm was measured by a multifunctional enzyme-labeled instrument (ThermoFisher, Waltham, MA, USA), and the cell viability rate was calculated as shown in Eq. (1):

$$\text{Cell viability}\ (\%) = (\text{OD}_{\text{test}} - \text{OD}_{\text{zero}}) / (\text{OD}_{\text{control}} - \text{OD}_{\text{zero}}) \times 100 \quad (1)$$

where OD_{test} is the administered group, $OD_{control}$ is the control group, and OD_{zero} is the blank group.

Next, a scratch assay was performed to evaluate the pro-migration ability of G^+. Briefly, 4T1 cells and G^+-4T1 cells (3×10^5 cells/well) were seeded into 24-well plates. Then, the plates were scratched using a pipette tip. The area of the scratches for each group at different times was measured.

2.5. G^+-4T1 cells uptake of DFTV

To detect the cellular uptake of DFTV, G^+-4T1 cells were incubated with free DOX and DFTV (equivalent to 1 μg/mL DOX) for 2, 6, and 12 h. The fluorescence of DOX in G^+-4T1 cells was observed using a flow cytometry assay. Furthermore, the intracellular co-localization of DFTV or DOX with G^+ was observed by confocal laser scanning microscopy (CLSM 800, Zeiss, Germany). Firstly, G^+-4T1 cells (1.2×10^5 cells/well) were added to the confocal dish, and the FITC fluorescent dye was used to label G^+ (MOI = 200) for 4 h. Following the formation of covalent bonds between the isothiocyanate group of FITC and the amino or sulfhydryl groups on the bacteria, the bacteria exhibited a green fluorescence signal. Subsequently, both DOX and DFTV (equivalent to 5 μg/mL DOX) were added and co-incubated for 2 h. Images were acquired using CLSM.

2.6. In vitro antibacterial effect of DFTV

The suspension of *Staphylococcus xylosus* (*S. xylosus*) was diluted to a concentration of 1×10^6 colony-forming units (CFU)/mL in broth medium. Then, using the broth gradient dilution method, G^+ suspension was mixed with DFTV (0.68, 0.46, 0.30, 0.20, 0.14, 0.09, 0.06, and 0.04 μg/mL) or Van (10.25, 6.83, 4.56, 3.04, 2.03, 1.35, 0.90, and 0.60 μg/mL). The plates were incubated in the bacterial incubator for 18 h to examine the minimal inhibitory concentration (MIC_{50}). Moreover, the G^+ suspension (OD_{600} = 1.0) was incubated with equal volumes of Van, DOX, DOX + Van, DFTV, DFTV + Laser (1.5 W/cm^2, 5 min), DFTV + Fer-1 (Fer-1 = 10 μmol/L), DFTV + DFP (DFP = 100 μmol/L), and broth

(Control group) for 30 min (equivalent to DOX = 4.0 μg/mL). The bacterial suspension of each treatment group was diluted 10^5-fold, and 20 μL of the suspension was spread on nutrient agar plates. After incubation for 18 h, the plates were taken out for photography and colony counting. Regarding the DFTV anti-intracellular G^+ assay, 4T1 cells were incubated with G^+ (MOI = 20) for 8 h. Then, G^+-4T1 cells (4×10^5 cells/well) were incubated with DFTV, DFTV + Laser (1.5 W/cm^2, 5 min), DFTV + Fer-1, DFTV + DFP (equivalent to DOX = 2.0 μg/mL), and RPMI-1640 medium for 10 h and centrifuged (1000 rpm, 5 min) to remove the drug-containing media. The lysate of all group cells was diluted 10-fold with saline and then plated onto agar plates for bacterial colony counting. The bacterial viability was calculated as shown in Eq. (2):

$$\text{Bacterial viability}\ (\%) = \frac{\text{Count of bacteria in the drug administration group}}{\text{Count of bacteria in the control group}} \times 100 \quad (2)$$

2.7. Ferroptosis analysis of DFTV in G^+-4T1 cells

The ROS generation was detected by fluorescence imaging and flow cytometry assay with the DCFH-DA probe. Besides, the production of lipid peroxidation (LPO) was measured using Liperfluo fluorescent probes by flow cytometry assay. Sample groups were as follows: PBS, TA (0.7 μg/mL), Van (0.5 μg/mL), DOX (1.0 μg/mL), $FeSO_4$ (equivalent to 0.9 μg/mL Fe^{2+}), DFTV, DFTV + Fer-1 (Fer-1 = 10 μmol/L), DFTV + DFP (DFP = 100 μmol/L), and DFTV + Laser group (equivalent to DOX = 1 μg/mL). Meanwhile, the SOD-like activity of DFTV was evaluated using the total SOD assay kit with the nitroblue tetrazolium (NBT) method. All measurements were performed in cell-free solutions, following the manufacturer's instructions. In detail, the superoxide anion radical generated by the catalytic reaction between xanthine and xanthine oxidase reduced NBT to blue formazan, which exhibited the absorption peak at 560 nm. The SOD-like activity of DFTV effectively scavenged the superoxide anion radical, thereby inhibiting the formation of formazan. Specifically, different formulas (20 μL) were added to the 96-well plates. Then, NBT (160 μL) was added to the solution for 30 min and quantified at 560 nm with a multifunctional enzyme-labeled instrument (Thermo Fisher). The UV−Vis spectrophotometry was used to examine the intracellular nicotinamide adenine dinucleotide phosphate oxidases (NOXs) activity of DFTV. Briefly, various treatment groups of G^+-4T1 cells were lysed and centrifuged at 10,000 rpm for 5 min, and the supernatant was mixed with NADPH (250 μmol/L). The decrease in absorbance of all groups at 340 nm within 5 min was recorded. Besides, ·OH generation capacity was determined by UV−Vis spectrophotometer at 652 nm. Different concentrations of DFTV were added to solutions of 3,3',5,5'-tetramethylbenzidine (TMB, 10 mg/mL) and H_2O_2 (10 mmol/L) in phosphate buffer. The absorbance changes at 652 nm were monitored for 5 min. In addition, mitochondrial changes in 4T1 and G^+-4T1 cells after 12 h incubation with DFTV were observed.

2.8. In vitro tumor proliferation inhibition efficiency of DFTV

A series of concentrations of DOX, DFTV, DFTV + Laser, DFTV + Fer-1 (Fer-1 = 10 μmol/L), and DFTV + DFP (DFP = 100 μmol/L) were co-incubated with the cells for 24 h. For DFTV + Laser group, after incubation for 2 h, each well was irradiated at a power density of 1.5 W/cm^2 for 5 min, followed by an additional 22 h of incubation. Next, a CCK-8 solution (10%, *v*/*v*) was added, and absorbance at 450 nm of different treatment groups was measured.

Cell proliferation inhibition was determined by flow cytometry. Briefly, the G^+-4T1 cells (3×10^5 cells/well) were treated with PBS, DOX + Van, DFTV, DFTV + DFP (DFP = 100 μmol/L), and DFTV + Laser (equivalent to DOX = 5.0 μg/mL), respectively. Finally, the cells were stained with FVD eFluor®445 UV (dead-cells dye) for 30 min.

To visualize cytoskeletal protein in each treatment group, F-actin was stained with 488-phalloidin for 30 min. G^+ was stained with FITC for 30 min. Images were acquired using CLSM.

2.9. In vivo antibacterial and antitumor therapy of DFTV

Firstly, 4T1 cells were infected with G^+ at an MOI of 2 to produce G^+-4T1 cells. Next, a suspension of G^+-4T1 or naïve 4T1 cells (2×10^6/100 μL) was injected into the fourth mammary fat pad of BALB/c mice. To investigate G^+ colonization in 4T1 tumor, the tumor homogenate was spread on plates, and G^+ colonies were counted.

For antitumor efficacy of DFTV, mice were randomized into four groups when tumor volume reached about 50 mm^3 (n = 5). Mice received intravenously injections with saline (Control), physical mixture of free DOX and Van (DOX + Van), DFTV, and DFTV + Laser (equivalent to DOX dose of 5.0 mg/kg) on Days 0, 3, and 6. For DFTV + Laser group, tumors were irradiated with an 808 nm laser (1.0 W/cm^2, 5 min) 24 h post-injection. During the period of irradiation, the temperature of the irradiated area was monitored by infrared thermography. The tumor volume was measured daily, and the weight of the tumor-bearing mice was also recorded until Day 21. On Day 21, blood biochemistry tests were performed.

To evaluate the antitumor recurrence effect of DFTV, 90% of the tumor was surgically removed when it reached a tumor volume of approximately 200 mm^3, and the remaining 10% was a recurrence focus. After surgery, mice received identical treatments on Days 2, 4, and 6. During the irradiation period, the temperature of the irradiated area was monitored using infrared thermography. The tumor volume and the weight of the tumor-bearing mice were recorded until Day 12 after surgery.

The G^+ count of tumor homogenates was used to assess the antibacterial effect of the corresponding treatment. Furthermore, TLR2 expression in primary and post-surgical recurrent G^+-4T1 tumor was assessed by immunofluorescence. IL-6, IL-1β, and TNF-α levels were quantified by ELISA. In addition, tumor tissues from all treatment groups were subjected to H&E staining assay, TUNEL staining assay, Ki-67 staining assay, and $CD8^+$ T cells and Treg cells analysis. Besides, tumor tissues were lysed for GPX4 and F-actin protein expression analysis by Western blot assay. The metastasis in lung was analyzed by H&E staining.

2.10. Safety evaluation

Blood samples were collected from mice for liver function activity assay, including the levels of alanine aminotransferase (ALT) and

aspartate aminotransferase (AST). The major organs were sectioned and subjected to H&E staining.

2.11. Statistical analysis

The results were represented as means ± standard deviation (SD). Statistical comparisons were assessed by one-way ANOVA with multiple comparisons or two-tailed Student's *t*-test, as appropriate. $P < 0.05$ was considered statistically significant.

3. Results and discussion

3.1. Characterization of DFTV

DFTV was obtained through a two-step assembly process based on multidimensional intermolecular interactions. Firstly, DOX was self-assembled with TA to prepare DT, and $FeSO_4$ was self-assembled with Van to prepare FV. Then, DT was further assembled with FV to form DFTV nano-assemblies. As seen in Fig. 1A, DFTV had an irregular nanomorphology with a particle size of 168.23 ± 5.8 nm and a polydispersity index (PDI) of 0.12 ± 0.06. The drug loading efficiencies of DOX, Fe^{2+}, and Van in DFTV was 32.40 ± 0.4%, 31.10 ± 1.2%, and 22.20 ± 2.9%, respectively. Next, we investigated the crystal structure of DFTV through XRD patterns. Almost no peak in 2θ from 0 to 40° was observed in XRD patterns of DFTV, indicating that its amorphous nature (Fig. 1B). Meanwhile, DFTV showed good stability under storage conditions at 4 °C and under the conditions simulating the blood circulation system (Fig. 1C and Supporting Information Fig. S1). Subsequently, the drug release of DFTV in breast tumor homogenate and 4T1 cell homogenate was higher than that in serum (Supporting Information Fig. S2). This result suggested that DFTV had tumor microenvironment-responsive drug release properties. Besides, as a transition metal ion, Fe^{2+} has unsaturated d-orbitals. Accordingly, when Fe^{2+} was complexed with the phenolic compound TA, the 808 nm near-infrared laser absorption would trigger a d-orbital electron jump and lead to a PTT effect[20]. As expected, DFTV with a photothermal conversion efficiency (η) of 44.5% showed favorable photothermal effects (Fig. 1D and Supporting Information Figs. S3−S5). The photothermal stability of DFTV was also better than the classical photosensitizer indocyanine green (ICG) (Fig. 1E) since the stabilization of DFTV structures. Benefiting from the intersystem crossover (ISC) and Fenton reaction[21], DFTV + Laser could effectively generate ROS under the conditions of 808 nm laser (1.5 W/cm^2, 5 min) in the presence of H_2O_2 (5 mmol/L) (Fig. 1F). This contributed to its dual antibacterial and antitumor efficacy.

Subsequently, we explored the nano-assembly mechanisms of DFTV. As shown in Supporting Information Fig. S6, after adding SDS (hydrophobic force elimination)[22], NaCl (electrostatic force elimination)[23], and EDTA (coordination bond elimination)[24] to the DFTV solution, respectively, the precipitation stratification of the DFTV solution was evident. After adding the urea (hydrogen bond elimination)[25], the color of the DFTV solution became lighter. Besides, as shown in Supporting Information Fig. S7, after adding SDS, NaCl, EDTA, and urea, the characteristic peak of DFTV at 500 nm in UV−vis spectra exhibited a decrease or blue shift, and the particle sizes of DFTV noticeably increased. All these results indicated that hydrophobic, electrostatic, coordination interactions, as well as hydrogen bonding, were involved in the assembly of DFTV. In addition, the results of fluorescence spectrophotometry and UV−Vis spectrophotometry revealed that $\pi-\pi$ interaction also contributed to the assembly of DFTV. As shown in Fig. 1G, DOX had a firm fluorescence emission peak in the range of 500−700 nm. In contrast, the fluorescence of the emission bands in DFTV spectra almost disappeared. This was because the $\pi-\pi$ interaction-based assembly process in DFTV caused the excited energy of DOX to be transferred to TA through stacking between planes, inducing fluorescence quenching[26,27]. In UV−Vis spectrum of DFTV, the characteristic wavelength of DOX at 480 nm was red-shifted to 500 nm. Meanwhile, the absorption peak of DFTV at 500 nm broadened (Fig. 1H), which was caused by the bidentate chelation of Fe^{2+} with the hydroquinone site in the molecular structure of DFTV[27]. In FTIR of DFTV, the intensity of absorption peaks $\nu_{(O-H)}$ of TA at 3336 cm^{-1} was significantly weakened. Meanwhile, the intensity of absorption peaks $\nu_{(C-O)}$ of TA at 1195 cm^{-1} was weakened and blue-shifted to 1201 cm^{-1} (Fig. 1I). These results indicated the ligand interaction of Fe^{2+} with −OH in TA[28]. Moreover, the absorption peak of Van at 1659 cm^{-1} disappeared in the DFTV group. This might be attributed to that the amino group of Van potentially provided hydrogen bonding interactions and electrostatic interaction sites to assemble with other molecules. The characteristic peaks of DOX at 968 cm^{-1}, 991 cm^{-1}, and 1006 cm^{-1} ($\delta_{(Ar-H)}$) were blue-shifted to 986 cm^{-1}, 1015 cm^{-1}, and 1033 cm^{-1} in DFTV group, also confirming that electrostatic interactions were involved in the assembly of DFTV. After parsing the force types that drive DFTV assembly, microscale thermophoresis (MST) was employed to analyze force strength between the different components of DFTV. The K_d value represented the affinity of the interaction force between molecules. The larger the K_d value, the lower the intermolecular affinity. As shown in Fig. 1J and Supporting Information Table S1, $K_{d\ (DOX-TA)} < K_{d\ (DOX-Van)} < K_{d\ (DOX-FeSO4)}$ and $K_{d\ (DT-FV)} < K_{d\ (DT-FeSO4)} < K_{d\ (DT-Van)}$ at 298 K. These results explained why the best DFTV could be obtained by using the two-step method of first assembling the DT and FV and then assembling the DT with the FV. Meanwhile, the thermodynamic parameters obtained by the linear relationship of the van't Hoff plot (Supporting Information Fig. S8) also verified the types of intermolecular forces of DFTV[29,30]. The interaction between DOX and TA was a spontaneous exothermic process to form hydrogen bonds because the free energy, enthalpies (ΔH), and entropy (ΔS) were less than zero. Although DT and FV interaction was also a spontaneous exothermic process, ΔS was greater than zero, which meant that electrostatic interaction participated in this assembly (Supporting Information Table S2). Finally, we further analyzed the relative positions of each molecule after DFTV assembly. As shown in DSC data, the endothermic peak of DFTV at 79.66 °C could be attributed to the peak of Van at 84.70 °C, but the typical peaks of DOX, TA, and $FeSO_4$ in DFTV disappeared (Fig. 1K). This might be attributed to DOX, TA, and $FeSO_4$, which were inside the self-assembly system, while Van was wrapped around them.

3.2. Antibacterial efficacy and mechanisms of DFTV against G^+

Next, we employed *S. xylosus*, a key G^+ that colonized breast tumor cells to promote breast cancer development[5], as the G^+ model to test the antibacterial capacity of DFTV. As exhibited in Supporting Information Table S3, the results of antibacterial experiments showed that the MIC_{50} of Van (2.73 μg/mL) was approximately 10

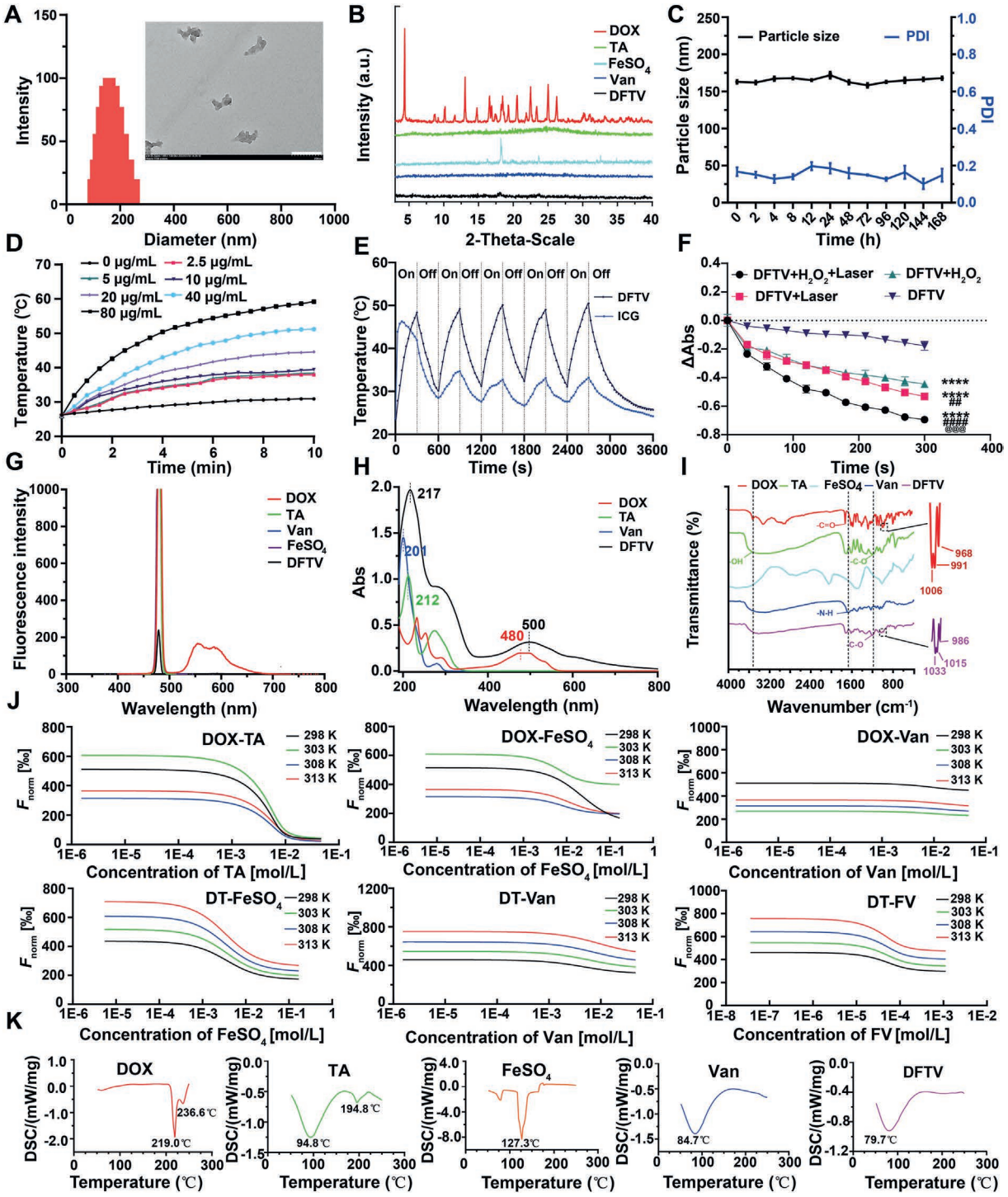

Figure 1 (A) Particle size and the TEM image of DFTV. Scale bar = 200 nm. (B) XRD analysis of DOX, TA, $FeSO_4$, Van, and DFTV. (C) Particle size and PDI changes of DFTV at 4 °C within 7 days. (D) Temperature elevation of DFTV at different concentrations (equivalent to Fe^{2+} concentration) under 808 nm laser irradiation (1.5 W/cm^2, 10 min). (E) Photothermal stability of DFTV and ICG solution during 5 rounds of laser ($C_{Fe}{}^{2+}$ = 40 μg/mL and C_{ICG} = 16 μg/mL, 808 nm, 1.5 W/cm^2, 10 min/round). (F) 1,3-Diphenylisobenzofuran (DPBF) was used as a ROS probe to detect the level of ROS after different treatments. $^{****}P < 0.0001$ *vs.* DFTV, $^{\#\#}P < 0.01$ and $^{\#\#\#\#}P < 0.0001$ *vs.* DFTV + H_2O_2; $^{@@@@}P < 0.001$ *vs.* DFTV + Laser. (G) Fluorescent spectra of DOX, TA, Van, $FeSO_4$, and DFTV. (H) UV−Vis spectra of DOX, TA, Van, and DFTV. (I) FTIR spectra of DOX, TA, $FeSO_4$, Van, and DFTV. (J) Binding curves of DOX or DT with different ligands at a series of temperatures obtained by MST. (K) The DSC thermograms of DOX, TA, $FeSO_4$, Van, and DFTV. Error bars represent mean ± SD (n = 3).

times higher than that of DFTV (0.28 μg/mL). Furthermore, the colony-forming assay revealed that compared to DOX + Van group without ferroptosis therapy activity, the antibacterial activity of DFTV group was significantly improved (Fig. 2A and B). Moreover, we also observed that the bacterial viability of DFTV + Laser group was further reduced by 59.79% compared to DFTV group. This enhancement might be attributed to phototherapy upregulating ferroptosis marker LPO levels through extra ROS generation, thereby promoting the antibacterial treatment efficacy of DFTV (Fig. 2C and D, Supporting Information Figs. S9 and S10). Besides, DFTV also demonstrated this advantageous antibacterial capacity in intracellular G^+. As shown in Supporting Information Fig. S11, G^+-4T1 cells were employed as the cell model, which was successfully established by incubating G^+ with 4T1 cells. Compared to other treatment groups, the number of intracellular G^+ clones in DFTV+Laser group was the lowest (Fig. 2E and F). The superior antibacterial effect of DFTV could be immediately diminished once different ferroptosis inhibitors, such as Fer-1 or DFP, were added, indicating that ferroptosis therapy mediated by DFTV provided high performance with antibacterial activity.

Besides, this superior antibacterial effect of DFTV also might be attributed to that DFTV could effectively enter G^+-4T1 cells (Fig. 2G−I), thereby overcoming the biofilm permeability barrier for antibiotics to enter bacteria within tumor cells. Above all, DFTV significantly improved the antibacterial efficiency of antibiotic therapy and overcame the deficiency of antibiotic monotherapy for intracellular G^+ by mediating ferroptosis therapy, phototherapy, as well as improving the targeted drug delivery efficiency of antibiotics to G^+ colonizing in tumor cells (Fig. 2J).

3.3. Ferroptosis-based antiproliferative and antimetastatic effects of DFTV against G^+-4T1 cells

DFTV-mediated ferroptosis also exert a potent antitumor activity, particularly against G^+-4T1 cells. The IC_{50} values of DFTV against 4T1 cells were reduced compared to DOX group, which rebounded after adding Fer-1 and DFP (Fig. 3A and Supporting Information Table S4). We also investigated the cytotoxicity of DFTV against G^+-4T1 cells. As shown in Supporting Information Figs. S12 and S13 and Fig. 3B, G^+ invasion could significantly promote the proliferation of 4T1 cells ($P < 0.05$), while DFTV + Laser treatment had a stronger fluorescence intensity of dead cells than G^+-4T1 cells ($P < 0.0001$). Notably, adding DFP significantly weakened the cytotoxicity of the DFTV group, indicating that ferroptosis played an irreplaceable role in inhibiting proliferation of G^+-4T1 cells. Furthermore, the ROS and LPO levels were evaluated to validate the effect of ferroptosis. Compared to other groups, the DFTV + Laser group had the most vigorous ROS and LPO generation levels (Fig. 3C and D, Supporting Information Figs. S14 and S15). In contrast, the ROS and LPO levels were markedly inhibited in the group using Fer-1 or DFP. Moreover, the ability of DFTV to induce ROS and LPO generation levels in 4T1 cells was consistent with those obtained in G^+-4T1 cells (Fig. 3E and Supporting Information Figs. S16 and S17). Meanwhile, another ferroptosis marker, GPX4, was also detected through Western blot assay. Compared to Control group, DFTV ($P < 0.05$) and DFTV + Laser ($P < 0.01$) could significantly downregulate the GPX4 expression, while DOX + Van group did not (Supporting Information Fig. S18). This result further confirmed that DFTV induced a reduction in cellular antioxidant capacity to promote ferroptosis *in vivo*.

Besides, DFTV treatment mediated ferroptosis in 4T1 cells and G^+-4T1 cells also induced changes in mitochondrial morphology, which was another hallmark phenomenon of ferroptosis. When ferroptosis occurred, mitochondrial shrinkage, cristae reduction, and outer membrane rupture were observed[20,31−33]. As shown in Fig. 3F and G and Supporting Information Figs. S19 and S20, the mitochondria of 4T1 cells were characterized with a clear and intact membrane structure and cristae. In contrast, DFTV-treated cells showed a remarkable decrease in mitochondrial length-diameter and cristae, as well as rupture of the mitochondrial outer membrane. More interestingly, besides the potent proliferation inhibition effect against G^+-4T1 cells described above, DFTV also effectively inhibited the migration of G^+-4T1 cells. As shown in Fig. 3H and I, G^+ invasion could significantly promote 4T1 cell migration, while DFTV treatment significantly inhibited this phenomenon. In detail, DFTV group (6.66 ± 3.1%) and DFTV + Laser group (4.44 ± 4.9%) showed lower migration rates than other groups in the migration assay. Furthermore, the CLSM images showed that compared with 4T1 cells, filopodia (white arrows) were visible on the cell membrane of G^+-4T1 cells, and the filopodia disappeared after DFTV treatment (Fig. 3J).

We also observed that DFTV treatment could lead to intracellular stress fibers becoming unclear, which was proved by a notable reduction in the fluorescence intensity of F-actin (Fig. 3J). Furthermore, the results of Western blot assay confirmed that DFTV and DFTV + Laser treatments significantly reduced the expression levels of F-actin in G^+-4T1 tumors (Fig. S18). All these results demonstrated that DFTV could weaken the movement and deformation ability of G^+-4T1 cells by reducing the formation of G^+-induced pseudopods and the expression of stress fibers. This potentially helped to effectively inhibit tumor metastasis.

Notably, antibacterial effect, antitumor cell proliferation, and antimigration effect described above were closely related to the contribution of DFTV-mediated ferroptosis therapy. Based on this, we further examined the ability of DFTV to induce intracellular biological oxidation-reduction cascade reactions. As shown in Fig. 3K, DFTV had a similar ability to activate NOXs as DOX in G^+-4T1 cellular environment. The NBT assay confirmed that DFTV maintained the SOD-like enzyme activity (Fig. 3L). In addition, in order to detect the ·OH production effect of DFTV, the TMB assay was also conducted. As shown in Supporting Information Fig. S21, an increase in TMB absorbance was observed with an elevation in DFTV concentration, indicating that DFTV possessed the capability to oxidize H_2O_2 and generate ·OH. These results revealed that these two significant steps to trigger and connect the cascade reactions could efficiently occur as designed intracellularly, which provided a strong guarantee for the Fenton reaction to generate ROS (Supporting Information Fig. S22).

3.4. In vivo antitumor capability of DFTV against G^+-4T1 tumor-bearing mice

The above excellent therapeutic effect of DFTV against G^+-4T1 cells provided us with great confidence in further evaluating its therapeutic effect against breast cancer *in vivo*. Firstly, we established the G^+-colonized breast cancer model (G^+-4T1 tumor). The G^+-4T1 tumor exhibited remarkably more rapid tumor growth and higher tumor weights than the 4T1 tumor (Supporting Information Fig. S23A and S23B). Meanwhile, H&E staining showed that the area of lung metastasis in the G^+-4T1 tumor

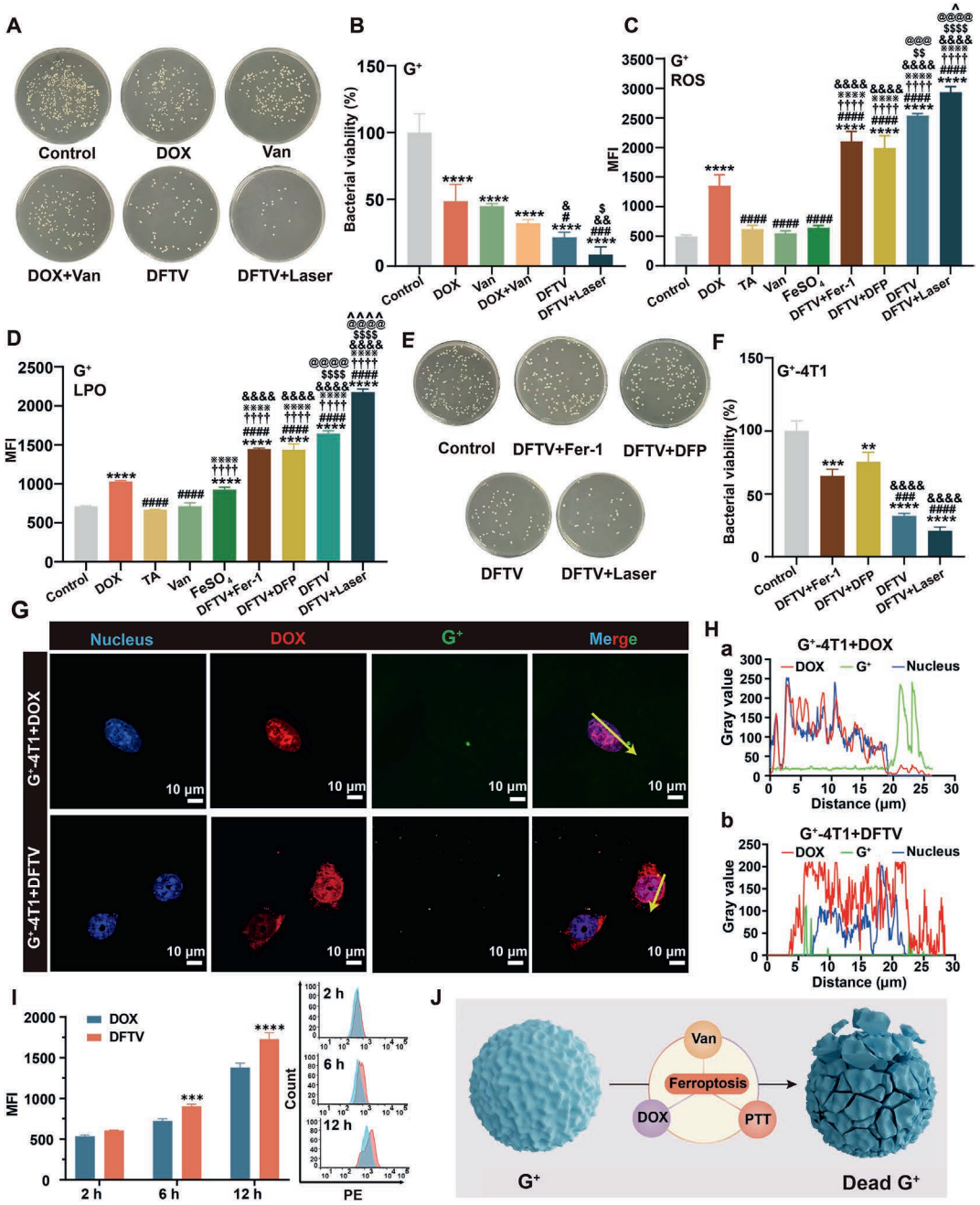

Figure 2 (A) Colony images and (B) quantification of planktonic G^+ viability after treatments with PBS, DOX, Van, DOX + Van, DFTV and DFTV + Laser. $^{****}P < 0.0001$ *vs.* Control; $^{\#}P < 0.05$ and $^{\#\#\#}P < 0.001$ *vs.* DOX; $^{\&}P < 0.05$ and $^{\&\&}P < 0.01$ *vs.* Van; $^{\$}P < 0.05$ *vs.* DOX + Van. (C) The ROS production in G^+ after different treatments, as assessed by flow cytometry assay. (D) The LPO level in G^+ after different treatments, as assessed by flow cytometry assay. $^{****}P < 0.0001$ *vs.* Control; $^{\#\#\#\#}P < 0.0001$ *vs.* DOX; $^{\dagger\dagger\dagger\dagger}P < 0.0001$ *vs.* TA; $^{※※※※}P < 0.0001$ *vs.* Van; $^{\&\&\&\&}P < 0.0001$ *vs.* $FeSO_4$; $^{\$\$}P < 0.01$ and $^{\$\$\$\$}P < 0.0001$ *vs.* DFTV + Fer-1; $^{@@}P < 0.001$ and $^{@@@@}P < 0.0001$ *vs.* DFTV + DFP; $^{\wedge}P < 0.05$ and $^{\wedge\wedge\wedge\wedge}P < 0.0001$ *vs.* DFTV. (E) Colony images and (F) quantification of intracellular G^+ viability. $^{**}P < 0.01$ and $^{***}P < 0.001$, $^{****}P < 0.0001$ *vs.* Control; $^{\#\#\#}P < 0.001$ and $^{\#\#\#\#}P < 0.0001$ *vs.* DFTV + Fer-1, $^{\&\&\&\&}P < 0.0001$ *vs.* DFTV + DFP. (G) CLSM images of G^+-4T1 cells were incubated with DOX and DFTV for 2 h. The yellow fluorescence signal indicated DFTV co-localized with intracellular G^+. (H) Co-localization fluorescence intensity profiles along the yellow line for G^+-4T1+DOX (a) and G^+-4T1+DFTV (b). (I) Intracellular uptake of DOX and DFTV nano-assembly in G^+-4T1 cells, as assessed by flow cytometry. $^{***}P < 0.001$ *vs.* DOX (6 h) and $^{****}P < 0.0001$ *vs.* DOX (12 h). (J) Schematic diagram of the antibacterial mechanism of DFTV. Error bars represent mean ± SD ($n = 3$). Statistical analysis was performed using one-way ANOVA with Tukey's multiple comparisons test.

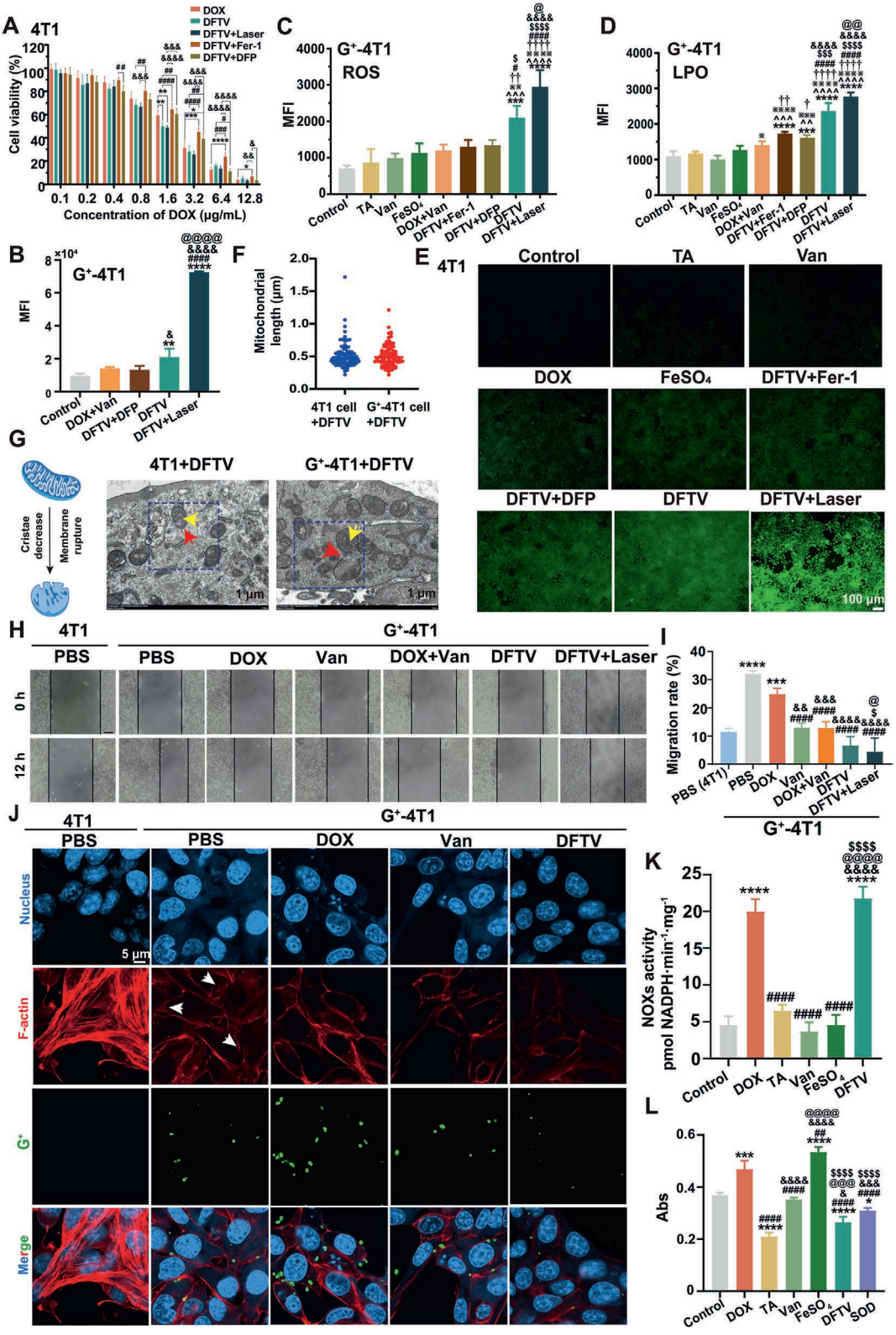

Figure 3 (A) Cytotoxicity assay of DOX, DFTV, DFTV + Laser, DFTV + Fer-1, and DFTV + DFP against 4T1 cells for 24 h ($n = 6$). (B) The fluorescence intensity of dead cells in G^+-4T1 cells treated with different formulas, as assessed by flow cytometry. (C) ROS and (D) LPO levels in G^+-4T1 cells with different formulas, as assessed by flow cytometry. $^{**}P < 0.01$, $^{***}P < 0.001$ and $^{****}P < 0.0001$ *vs.* Control; $^{\wedge\wedge}P < 0.01$, $^{\wedge\wedge\wedge}P < 0.001$ and $^{\wedge\wedge\wedge\wedge}P < 0.0001$ *vs.* TA; $^{※}P < 0.05$, $^{※※}P < 0.01$ $^{※※※}P < 0.001$ and $^{※※※※}P < 0.0001$ *vs.* Van; $^{\dagger}P < 0.05$, $^{\dagger\dagger}P < 0.01$ and $^{\dagger\dagger\dagger\dagger}P < 0.0001$ *vs.* $FeSO_4$; $^{\#}P < 0.05$ and $^{\#\#\#\#}P < 0.0001$ *vs.* DOX + Van; $^{\$}P < 0.05$, $^{\$\$\$}P < 0.001$ and $^{\$\$\$\$}P < 0.0001$ *vs.* DFTV + Fer-1; $^{\&}P < 0.05$, $^{\&\&\&\&}P < 0.0001$ *vs.* DFTV + DFP; $^{@}P < 0.05$ and $^{@@}P < 0.01$ and $^{@@@@}P < 0.0001$ *vs.* DFTV. (E) ROS production in 4T1 cells with different formulas as observed by fluorescence microscope. (F) Mitochondrial length-diameter analysis and (G) bio-TEM images of 4T1

group was 2.48-fold higher than that of the 4T1 tumor group (Supporting Information Fig. S24). Moreover, as shown in Supporting Information Fig. S25A, the TLR2 expression in the G^+-4T1 tumor significantly increased, further leading to elevated expression of IL-6, IL-1β, and TNF-α (Fig. S25B−S25D). All these results also indicated that the increase in bacterial abundance in tumor tissues could lead to increased levels of IL-6, IL-1β, and TNF-α, which were also positively correlated with the risk of tumor proliferation and metastasis[34−36]. Accordingly, inhibiting intracellular G^+ and blocking these pathways were essential to close gaps in breast cancer therapy. As shown in Fig. 4A and B and Supporting Information Figs. S26 and S27, compared to DOX + Van group, which combined chemotherapy with conventional antibiotics, the antitumor efficiency of DFTV and DFTV + Laser was significantly improved after therapeutic regimens with the same administration. Especially, DFTV + Laser group showed sustained tumor proliferation inhibition efficacy after treatment (Fig. 4C) and further showed a significantly higher tumor inhibition ratio than DFTV ($P < 0.0001$) (Fig. 4D). Furthermore, H&E analysis, TUNEL assay, and Ki-67 analysis showed that the DFTV + Laser group had the most obvious cell apoptosis and the most significantly decreased number of Ki-67 positive cells (Fig. 4E and Supporting Information Fig. S28). Besides, as shown in Fig. 4F and G, the DFTV + Laser group presented the least lung metastasis areas. Consistent with antitumor effect results, compared to DOX + Van group, both DFTV and DFTV + Laser groups also showed a stronger antibacterial effect to intratumor colonizing G^+ (Fig. 4H and I). These results also emphasized that DFTV with effective ferroptosis therapy had overcome the apparent limitations of conventional antibiotic therapy for intratumoral bacteria. Benefiting from this potent antibacterial effect, the DFTV + Laser group showed the best comprehensive regulation effect on downregulation of IL-6, IL-1β, and TNF-α (Fig. 4J−L). As reported, inflammatory cytokines such as IL-1, TNF, and IL-6 were upregulated in tumor microenvironment (TME), playing a key role in tumor progression and immune evasion[37]. Our results showed that DFTV + Laser treatment led to a significant reduction in these cytokines, suggesting that the elimination of G^+ could disrupt this inflammatory cascade, thereby potentially mitigating tumor progression. Besides, we also detected the levels of $CD8^+$ T cells and Treg cells in tumors after different treatments. As illustrated in Supporting Information Fig. S29, $CD8^+$ T cell expression was higher in DFTV and DFTV+Laser groups compared to DOX + Van group ($P < 0.0001$). Meanwhile, the lowest levels of Treg cells in tumor tissues were observed following DFTV + Laser treatment. All these results indicated that DFTV + Laser also presented a substantial beneficial remodeling effect on the tumor immune microenvironment.

3.5. Postoperative therapeutic effects of DFTV against G^+-4T1 tumor-bearing mice

Clinically, most breast cancer patients undergo surgical treatment. However, tumor resection carried a high risk of recurrence and often had a poor prognosis[38,39]. Accordingly, to further simulate the clinical breast cancer treatment regimen, we also constructed a G^+-4T1 postoperative recurrence tumor model to further validate the antitumor effect of DFTV. The tumor growth and tumor weight of the G^+-4T1 tumors after surgery were significantly higher than those of the 4T1 tumors (Supporting Information Fig. S30A and S30B). This was because G^+ could still be detected from the postoperative residual tumor cells even under conditions of adequate surgical sterilization (Supporting Information Fig. S31). Besides, we found that G^+ also increased the TLR2 as well as IL-6, TNF-α, and IL-1β expression in G^+-4T1 postoperative recurrence tumor models (Supporting Information Fig. S32), which might explain why G^+ had a pro-tumor recurrence effect. Fortunately, DFTV treatment remained effective in inhibiting G^+-4T1 tumor postoperative recurrence. As shown in Fig. 5A−D, Supporting Information Figs. S33 and S34, DFTV + Laser group with an inhibition rate of 84.97%, exerted the strongest antitumor effect against G^+-4T1 postoperative recurrence tumor. The results of H&E assay, Ki-67 assay, and TUNEL assay also showed that DFTV + Laser group had the best results in inducing necrosis and apoptosis, as well as leading to the best prognosis (Fig. 5E and Supporting Information Fig. S35). In addition, as shown in Fig. 5F and G, DFTV and DFTV + Laser treatment also significantly reduced lung metastasis ($P < 0.05$). The remarkable inhibitory effects of DFTV in preventing postoperative recurrence and metastasis is attributed to its excellent antibacterial capacity. Compared to Control group, the bacterial density of tumor homogenate in the DFTV + Laser group was reduced by about 98.9% (Fig. 5H and I). Moreover, the inhibition of intratumor colonization of G^+ also further reduced the expression of IL-6, IL-1β, and TNF-α in G^+-4T1 postoperative recurrence tumor model (Fig. 5J−L). Elevated levels of these inflammatory cytokines support tumor cell survival[40-42] and their reduction through the inhibition of intratumor colonization of G^+ may contribute to suppressing postoperative tumor recurrence.

Finally, we preliminarily evaluated the safety of DFTV treatment. No significant mice body weight changes were detected in DFTV treatment group after multiple-dose administration (Supporting Information Figs. S36 and S37). Besides, there were no significant differences in the levels of liver function indicators ALT and AST between the four groups (Supporting Information Figs. S38 and S39). Pathologic evaluations also showed no cardiac, renal, and hepatic toxicity in DFTV + Laser group (Supporting Information Figs. S40 and S41).

cells + DFTV group and G^+-4T1 cells + DFTV group. The yellow arrow indicates the mitochondrial cristae and the red arrow indicates the mitochondrial outer membrane rupture. The blue dashed box indicates regions of interest ($n = 50$). (H) Migration images and (I) migration rates of cells treated with different formulas. $^{***}P < 0.001$ and $^{****}P < 0.0001$ *vs.* PBS (4T1); $^{\#\#\#\#}P < 0.0001$ *vs.* PBS (G^+-4T1); $^{\&\&}P < 0.01$, $^{\&\&\&}P < 0.001$ and $^{\&\&\&\&}P < 0.0001$ *vs.* DOX; $^{\$}P < 0.05$ *vs.* Van; $^{@}P < 0.05$ *vs.* DOX + Van. Scale bar = 100 μm. (J) Phalloidin staining of different treatment groups of cytoskeletal proteins. Red, F-actin, Green, fluorescein isothiocyanate (FITC) probe detecting G^+ (the white arrow indicates filopodia). (K) NOXs activating ability of different treatment groups. (L) NBT assay to test the absorbance of methyl hydrazone. $^{*}P < 0.05$, $^{***}P < 0.001$ and $^{****}P < 0.0001$ *vs.* Control; $^{\#\#}P < 0.01$ and $^{\#\#\#\#}P < 0.0001$ *vs.* DOX; $^{\&}P < 0.05$ and $^{\&\&\&}P < 0.001$, $^{\&\&\&\&}P < 0.0001$ *vs.* TA; $^{@@@}P < 0.001$ and $^{@@@@}P < 0.0001$ *vs.* Van; $^{\$\$\$\$}P < 0.0001$ *vs.* $FeSO_4$. Error bars represent mean ± SD ($n = 3$). Statistical analysis was performed using one-way ANOVA with Tukey's multiple comparisons test.

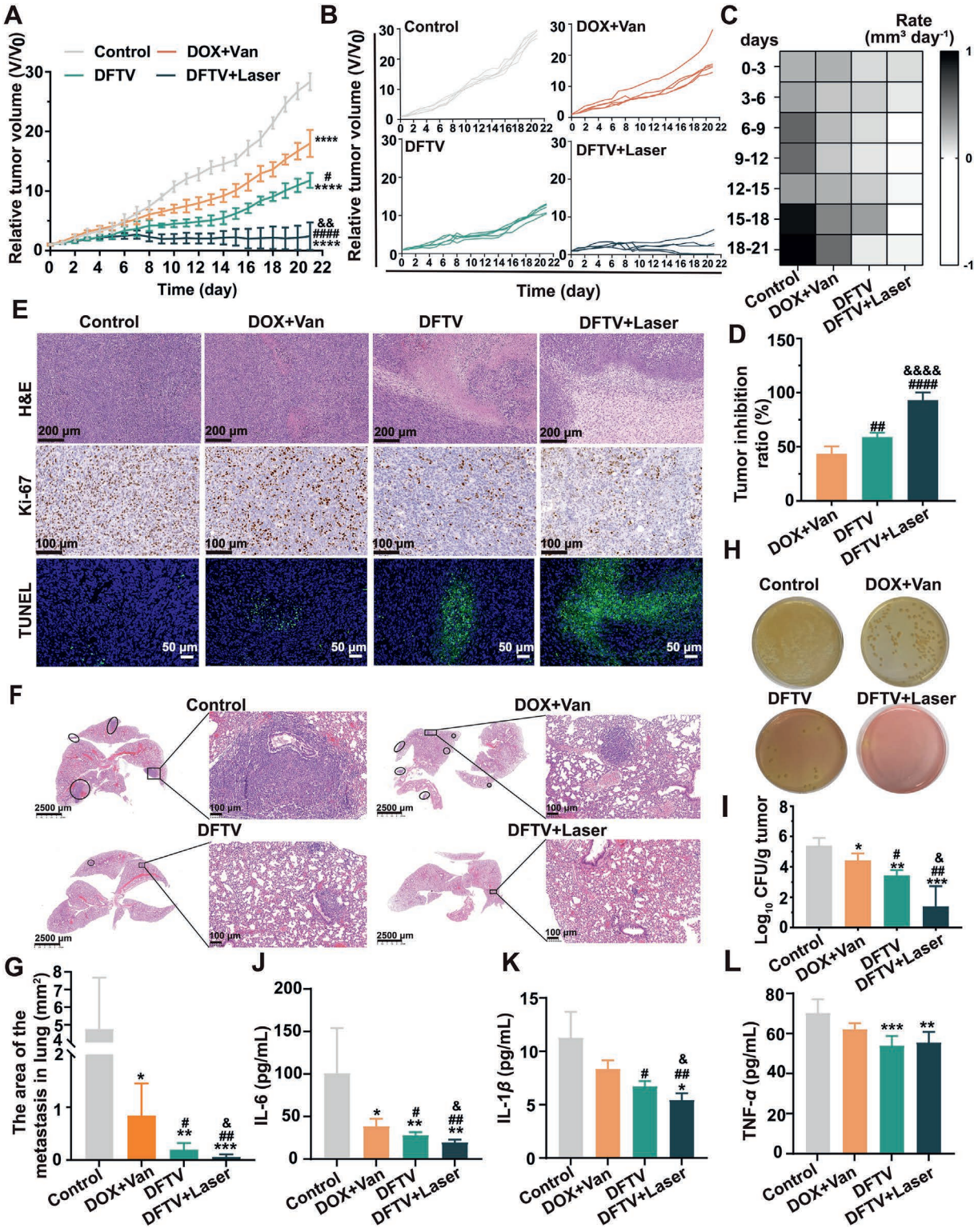

Figure 4 (A) Relative tumor growth curves of G^+-4T1 tumors after treatment with saline, DOX + Van, DFTV, and DFTV + Laser (1.0 W/cm^2, 5 min). (B) Relative tumor growth curves of each G^+-4T1 tumor-bearing mouse. (C) Tumor growth rates of G^+-4T1 tumors with different formulas. (D) The tumor inhibition ratio in G^+-4T1 tumors with different formulas. (E) H&E staining, Ki-67 staining, and TUNEL staining images with different formulas. (F) H&E staining images of lung tissues in G^+-4T1 tumor-bearing mice with different formulas. The circled areas indicate obvious lung metastases. (G) Quantitative analysis of lung metastases area with different formulas. (H) G^+ colonies image of G^+-4T1 tumor homogenate with different formulas. (I) Statistical analysis of CFUs in G^+-4T1 tumors with different formulas. The serum IL-6 (J), IL-1β (K), and TNF-α (L) levels with different formulas. $^*P < 0.05$, $^{**}P < 0.01$, $^{***}P < 0.001$ and $^{****}P < 0.0001$ *vs.* Control; $^{\#}P < 0.05$, $^{\#\#}P < 0.01$ and $^{\#\#\#\#}P < 0.0001$ *vs.* DOX + Van; $^{\&}P < 0.05$, $^{\&\&}P < 0.01$ and $^{\&\&\&\&}P < 0.0001$ *vs.* DFTV. Error bars represent mean ± SD ($n = 5$). Statistical analysis was performed using one-way ANOVA with Tukey's multiple comparisons test.

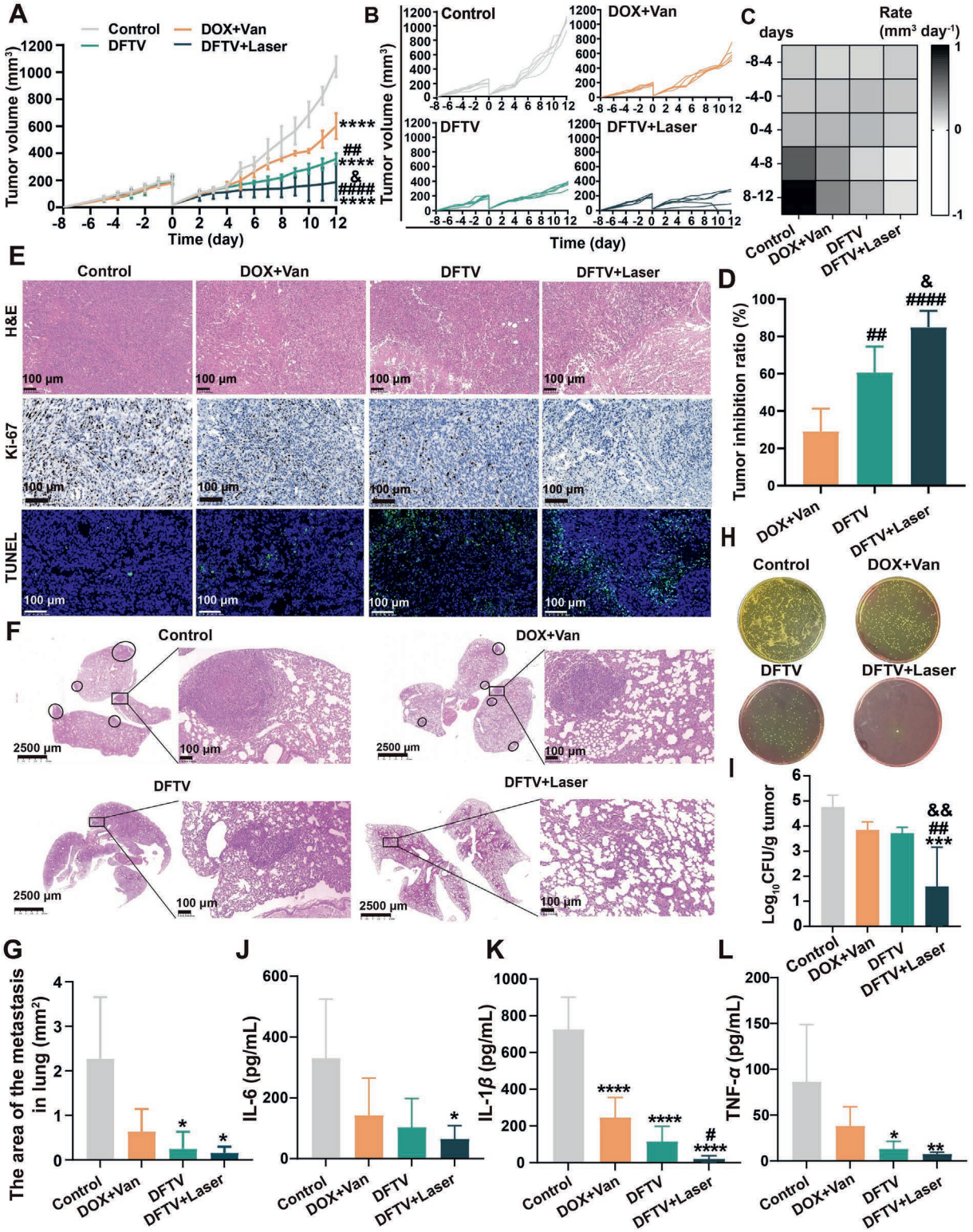

Figure 5 (A) G^+-4T1 postoperative recurrence tumor growth curves after treatment with saline, DOX + Van, DFTV, and DFTV + Laser (1.0 W/cm^2, 5 min). (B) Tumor growth curves of each G^+-4T1 postoperative recurrence tumor-bearing mice. (C) The tumor growth rates of G^+-4T1 postoperative recurrence tumors with different formulas. (D) The tumor inhibition ratios in G^+-4T1 postoperative recurrence tumors with different formulas. (E) H&E staining, Ki-67 staining, and TUNEL staining images of G^+-4T1 postoperative recurrence tumor with different formulas. (F) H&E staining images of lung tissues in G^+-4T1 postoperative recurrence tumor-bearing mice with different formulas. The circled areas indicate obvious lung metastases ($n = 3$). (G) Statistical analysis of the area of lung metastases in different formulas. (H) G^+ colony images of G^+-4T1 postoperative recurrence tumors homogenate with different formulas. (I) Statistical analysis of CFUs with different formulas. Serum IL-6 (J), IL-1β (K), and TNF-α (L) levels in G^+-4T1 postoperative recurrence tumor-bearing mice with different formulas. $^*P < 0.05$, $^{**}P < 0.01$ $^{***}P < 0.001$ and $^{****}P < 0.0001$ *vs.* Control; $^{\#}P < 0.05$, $^{\#\#}P < 0.01$ and $^{\#\#\#\#}P < 0.0001$ *vs.* DOX + Van; $^{\&}P < 0.05$ and $^{\&\&}P < 0.01$ *vs.* DFTV. Error bars represent mean ± SD ($n = 5$). Statistical analysis was performed using one-way ANOVA with Tukey's multiple comparisons test.

4. Conclusions

G^+ in breast tumor cells could accelerate tumor growth, recurrence, and metastasis by activating inflammatory pathways including TLR2-IL-6, IL-1β, and TNF-α and remodeling tumor cytoskeleton proteins, thus undermining breast cancer therapy. Here, the DFTV-induced ferroptosis significantly boosted the therapy of G^+-colonized breast cancer by effectively inhibiting intratumoral G^+, which would further reduce systemic inflammation and tumor cell motility. Our design also revealed that ferroptosis therapy had the unique advantage of reinforcing the antibacterial treatment efficiency against intracellular bacteria, which was particularly useful for overcoming the current drawbacks of antibiotic-based antibacterial treatments against bacteria colonized within tumor cells.

Acknowledgments

This project was supported by the National Natural Science Foundation of China (No. 82173754).

Author contributions

Yao Qi: experiments, writing-original draft, data curation, methodology and writing-review & editing. Yue Qiu: experiments, data curation, writing-original draft and methodology. Yuting Zhang: experiments, data curation, methodology and investigation. Liang Zhang: writing-review & editing, software and investigation. Hui Xiong: supervision, conceptualization, formal analysis and writing-review & editing. Jing Yao: conceptualization, funding acquisition, project administration and writing-review & editing.

Conflicts of interest

The authors declare no conflicts of interest.

Appendix A. Supporting information

Supporting information to this article can be found online at https://doi.org/10.1016/j.apsb.2026.01.027.

References

1. Chiba A, Bawaneh A, Velazquez C, Clear KYJ, Wilson AS, Howard-McNatt M, et al. Neoadjuvant chemotherapy shifts breast tumor microbiota populations to regulate drug responsiveness and the development of metastasis. *Mol Cancer Res* 2020;**18**:130−9.
2. Nejman D, Livyatan I, Fuks G, Gavert N, Zwang Y, Geller LT, et al. The human tumor microbiome is composed of tumor type-specific intracellular bacteria. *Science* 2020;**368**:973−80.
3. Matson V, Chervin CS, Gajewski TF. Cancer and the microbiome—influence of the commensal microbiota on cancer, immune responses, and immunotherapy. *Gastroenterology* 2021;**160**:600−13.
4. Bernardo G, Le Noci V, Ottaviano E, De Cecco L, Camisaschi C, Guglielmetti S, et al. Reduction of *Staphylococcus epidermidis* in the mammary tumor microbiota induces antitumor immunity and decreases breast cancer aggressiveness. *Cancer Lett* 2023;**555**:216041.
5. Fu AK, Yao BQ, Dong TT, Chen YY, Yao J, Liu Y, et al. Tumor-resident intracellular microbiota promotes metastatic colonization in breast cancer. *Cell* 2022;**185**:1356−72.e26.
6. Chen XY, Chen Y, Wang CC, Jiang YQ, Chu X, Wu F, et al. NIR-triggered intracellular H^+ transients for lamellipodia-collapsed anti-metastasis and enhanced chemodynamic therapy. *Angew Chem Int Ed* 2021;**60**:21905−10.
7. Li XC, Wang JL. Mechanical tumor microenvironment and transduction: cytoskeleton mediates cancer cell invasion and metastasis. *Int J Biol Sci* 2020;**16**:2014−28.
8. Kang X, Bu F, Feng W, Liu F, Yang X, Li H, et al. Dual-cascade responsive nanoparticles enhance pancreatic cancer therapy by eliminating tumor-resident intracellular bacteria. *Adv Mater* 2022;**34**:2206765.
9. Yu TC, Guo FF, Yu YN, Sun TT, Ma D, Han JX, et al. Fusobacterium nucleatum promotes chemoresistance to colorectal cancer by modulating autophagy. *Cell* 2017;**170**:548−63.e16.
10. Barcia-Macay M, Lemaire S, Mingeot-Leclercq MP, Tulkens PM, Van Bambeke F. Evaluation of the extracellular and intracellular activities (human THP-1 macrophages) of telavancin versus vancomycin against methicillin-susceptible, methicillin-resistant, vancomycin-intermediate and vancomycin-resistant *Staphylococcus aureus*. *J Antimicrob Chemother* 2006;**58**:1177−84.
11. Le Noci V, Guglielmetti S, Arioli S, Camisaschi C, Bianchi F, Sommariva M, et al. Modulation of pulmonary microbiota by antibiotic or probiotic aerosol therapy: a strategy to promote immunosurveillance against lung metastases. *Cell Rep* 2018;**24**:3528−38.
12. Geng SZ, Guo PK, Li XL, Shi Y, Wang J, Cao MN, et al. Biomimetic nanovehicle-enabled targeted depletion of intratumoral *Fusobacterium nucleatum* synergizes with PD-L1 blockade against breast cancer. *ACS Nano* 2024;**18**:8971−87.
13. Chen LF, Zhao R, Shen JJ, Liu NH, Zheng ZX, Miao Y, et al. Antibacterial fusobacterium nucleatum-mimicking nanomedicine to selectively eliminate tumor-colonized bacteria and enhance immunotherapy against colorectal cancer. *Adv Mater* 2023;**35**:2306281.
14. Zhou Y, Cai CY, Wang C, Hu GM, Li YT, Han MJ, et al. Ferric-loaded lipid nanoparticles inducing ferroptosis-like cell death for antibacterial wound healing. *Drug Deliv* 2023;**30**:1−8.
15. Shen XY, Ma RN, Huang YX, Chen L, Xu ZB, Li DD, et al. Nano-decocted ferrous polysulfide coordinates ferroptosis-like death in bacteria for anti-infection therapy. *Nano Today* 2020;**35**:100981.
16. An Y, Zhu JD, Liu F, Deng J, Meng X, Liu GQ, et al. Boosting the ferroptotic antitumor efficacy *via* site-specific amplification of tailored lipid peroxidation. *ACS Appl Mater Interfaces* 2019;**11**:29655−66.
17. Ma RN, Fang L, Chen L, Wang XN, Jiang J, Gao LZ. Ferroptotic stress promotes macrophages against intracellular bacteria. *Theranostics* 2022;**12**:2266−89.
18. Li ZQ, Chen LN, Chen C, Zhou YL, Hu DD, Yang JJ, et al. Targeting ferroptosis in breast cancer. *Biomark Res* 2020;**8**:58.
19. Lei G, Zhuang L, Gan B. Targeting ferroptosis as a vulnerability in cancer. *Nat Rev Cancer* 2022;**22**:381−96.
20. Xiong H, Wang C, Wang ZH, Jiang ZJ, Zhou JP, Yao J. Intracellular cascade activated nanosystem for improving ER+ breast cancer therapy through attacking GSH-mediated metabolic vulnerability. *J Control Release* 2019;**309**:145−57.
21. Ethirajan M, Chen Y, Joshi P, Pandey RK. The role of porphyrin chemistry in tumor imaging and photodynamic therapy. *Chem Soc Rev* 2011;**40**:340−62.
22. Han L, Liang S, Mu W, Zhang Z, Wang L, Ouyang S, et al. Amphiphilic small molecular mates match hydrophobic drugs to form nano-assemblies based on drug-mate strategy. *Asian J Pharm Sci* 2022;**17**:129−38.
23. Chung JE, Tan SS, Gao SJ, Yongvongsoontorn N, Kim SH, Lee JH, et al. Self-assembled micellar nanocomplexes comprising green tea catechin derivatives and protein drugs for cancer therapy. *Nat Nanotechnol* 2014;**9**:907−12.
24. He YJ, Xing L, Cui PF, Zhang JL, Zhu Y, Qiao JB, et al. Transferrin-inspired vehicles based on pH-responsive coordination bond to combat multidrug-resistant breast cancer. *Biomaterials* 2017;**113**:266−78.

25. Liu YF, Qi Y, Chen C, Jin YC, Du S, Qiao JN, et al. Platelet-mimetic nano-sensor for combating postoperative recurrence and wound infection of triple-negative breast cancer. *J Control Release* 2023;**362**: 396−408.
26. Zhang X, Zhang ZJ, Xu XH, Li YK, Li YC, Jian YT, et al. Bioinspired therapeutic dendrimers as efficient peptide drugs based on supramolecular interactions for tumor inhibition. *Angew Chem Int Ed* 2015;**54**: 4289−94.
27. Anand R, Borghi F, Manoli F, Manet I, Agostoni V, Reschiglian P, et al. Host−guest interactions in Fe(III)-trimesate MOF nanoparticles loaded with doxorubicin. *J Phys Chem B* 2014;**118**:8532−9.
28. Xu W, Lin Z, Pan S, Chen J, Wang T, Cortez-Jugo C, et al. Direct assembly of metal-phenolic network nanoparticles for biomedical applications. *Angew Chem Int Ed Engl* 2023;**135**:e202312925.
29. Mao YX, Yu LL, Yang R, Ma CG, Qu LB, Harrington PB. New peptide inhibitors modulate the self-assembly of islet amyloid polypeptide residues 11−20 *in vitro*. *Eur J Pharmacol* 2017;**804**:102−10.
30. Mao Y, Yu LL, Yang R, Ma CG, Qu LB, Harrington Pde B. New insights into side effect of solvents on the aggregation of human islet amyloid polypeptide 11−20. *Talanta* 2016;**148**:380−6.
31. Sang MM, Luo RJ, Bai YD, Dou J, Zhang ZT, Liu FL, et al. Mitochondrial membrane anchored photosensitive nano-device for lipid hydroperoxides burst and inducing ferroptosis to surmount therapy-resistant cancer. *Theranostics* 2019;**9**:6209−23.
32. Frey TG, Mannella CA. The internal structure of mitochondria. *Trends Biochem Sci* 2000;**25**:319−24.
33. Muñoz JP, Basei FL, Rojas ML, Galvis D, Zorzano A. Mechanisms of modulation of mitochondrial architecture. *Biomolecules* 2023;**13**: 1225.
34. Zhu Y, Mei Y, Baby N, Teo HY, Binte Hanafi Z, Mohd Salleh SN, et al. Tumor-mediated microbiota alteration impairs synaptic tagging/capture in the hippocampal CA1 area *via* IL-1β production. *Commun Biol* 2023;**6**:685.
35. Yang YZ, Weng WH, Peng JJ, Hong LM, Yang L, Toiyama YJ, et al. Fusobacterium nucleatum increases proliferation of colorectal cancer cells and tumor development in mice by activating toll-like receptor 4 signaling to nuclear factor-κB, and up-regulating expression of microRNA-21. *Gastroenterology* 2017;**152**:851−66.e24.
36. Johnson DE, O'Keefe RA, Grandis JR. Targeting the IL-6/JAK/STAT3 signalling axis in cancer. *Nat Rev Clin Oncol* 2018;**15**:234−48.
37. Li LH, Yu R, Cai TG, Chen Z, Lan M, Zou TT, et al. Effects of immune cells and cytokines on inflammation and immunosuppression in the tumor microenvironment. *Int Immunopharmacol* 2020;**88**: 106939.
38. Hiller JG, Perry NJ, Poulogiannis G, Riedel B, Sloan EK. Perioperative events influence cancer recurrence risk after surgery. *Nat Rev Clin Oncol* 2018;**15**:205−18.
39. Feng YZ, Zhang Z, Tang W, Dai YL. Gel/hydrogel-based *in situ* biomaterial platforms for cancer postoperative treatment and recovery. *Explorations* 2023;**3**:20220173.
40. Rašková M, Lacina L, Kejík Z, Venhauerová A, Skaličková M, Kolář M, et al. The role of IL-6 in cancer cell invasiveness and metastasis-overview and therapeutic opportunities. *Cells* 2022;**11**: 3698.
41. Bent R, Moll L, Grabbe S, Bros M. Interleukin-1 beta—a friend or foe in malignancies?. *Int J Mol Sci* 2018;**19**:2155.
42. Mantovani A, Allavena P, Sica A, Balkwill F. Cancer-related inflammation. *Nature* 2008;**454**:436−44.